**Journal of The Royal Society Interface**

# Supplementary Material

Association Between Erythrocyte Dynamics and Vessel Remodelling in Developmental Vascular Networks

Qi Zhou[1], Tijana Perovic[2,+], Ines Fechner[2,+], Lowell T. Edgar[3], Peter R. Hoskins[4,5], Holger Gerhardt[2,6,7,8], Timm Krüger[1,*], Miguel O. Bernabeu[3,*]

[1]School of Engineering, Institute for Multiscale Thermofluids, The University of Edinburgh, Edinburgh, UK
[2]Max-Delbrück-Center for Molecular Medicine in the Helmholtz Association (MDC), Berlin, Germany
[3]Centre for Medical Informatics, Usher Institute, The University of Edinburgh, Edinburgh, UK
[4]Centre for Cardiovascular Science, The University of Edinburgh, Edinburgh, UK
[5]Biomedical Engineering, University of Dundee, Dundee, UK
[6]Vascular Patterning Laboratory, Department of Oncology and Leuven Cancer Institute (LKI), KU Leuven, Belgium
[7]DZHK (German Center for Cardiovascular Research), Germany
[8]Berlin Institute of Health, Germany

[+]Equally contributing second authors (T.P. and I.F.)
[*]Corresponding authors: timm.krueger@ed.ac.uk (T.K.); miguel.bernabeu@ed.ac.uk (M.O.B.)

# S1 Simulations of cellular blood flow in microvascular networks of mouse retina

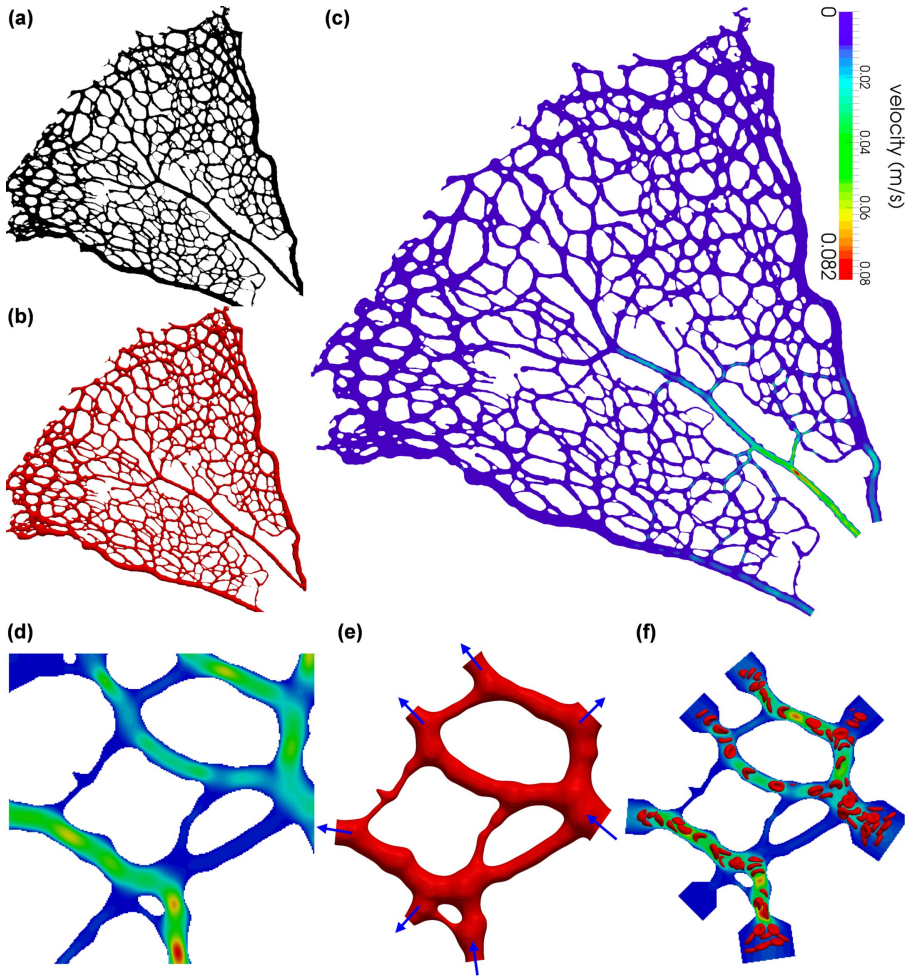


**Fig. S1. Procedure of model configuration and simulation setup for simulating cellular blood flow in designated regions of interest (ROIs) from the vascular plexus of a P5 mouse retina.** (**a**) Binary image of the vascular plexus stained for Col.IV. (**b**) Reconstructed whole-network geometry of the vessel luminal surface from (a). (**c**) Velocity field within the retinal network resolved by a flow model applying the non-Newtonian Carreau-Yasuda (NNCY) blood rheology in (b). (**d**) Zoomed in velocity field for a designated ROI in (c). (**e**) Clipped ROI subset from the whole-network geometry with inlets/outlets indicated by the inward/outward arrows. (**f**) Cellular flow simulation in the designated ROI imposing inflow/outflow and pressure boundary conditions extracted from (d).

The immersed-boundary-lattice-Boltzmann method (IB-LBM) [3] is employed to model blood flow as a suspension of deformable RBCs. The fluid flow governed by the Navier-Stokes equations is solved by the lattice-Boltzmann method (LBM) with standard D3Q19 lattice [4], BGK collision operator [5] and Guo's forcing scheme [6]. The no-slip condition on vessel walls is implemented with the Bouzidi-Firdaouss-Lallemand method

**Table S1. Key parameters of the whole-plexus simulation.** A simplified rheology model, namely the non-Newtonian Carreau-Yasuda (NNCY) model [1,2] is used.

| Parameter | Description | Value | Unit | Comment or reference |
|---|---|---|---|---|
| $D_{vessel}$ | vessel diameter | variable | $\mu$m | locally mapped by *PolNet* |
| $\Delta x$ | lattice size | 0.5 | $\mu$m | calculated by *PolNet* |
| $\Delta p$ | ocular perfusion pressure | 55 | mmHg | [2] |
| $\bar{u}$ | flow mean velocity | variable | m/s | averaged over cross-section |
| $Q$ | volume flow rate | variable | $m^3/s$ | $Q = \bar{u}\pi D_{vessel}^2/4$ |
| $\dot{\gamma}$ | shear rate | variable | 1/s | solved by *HemeLB* |
| $\eta(\dot{\gamma})$ | shear-thinning viscosity | variable | mPa s | $\eta(\dot{\gamma}) = \eta_\infty + \frac{(\eta_0-\eta_\infty)}{[1+(\lambda\dot{\gamma})^a]^{(1-n)a}}$ |
| $\eta_0$ | constant | 14.49 | mPa s | viscosity under low-shear |
| $\eta_\infty$ | constant | 3.265 | mPa s | viscosity under high-shear |
| $\lambda$ | constant | 0.1839 | s | fitting parameter |
| $n$ | constant | 0.4136 | - | fitting parameter |
| $a$ | constant | 2.707 | - | fitting parameter |

(BFL) [7]. Open boundaries are handled with the Ladd implementation of velocity boundary conditions [8] for control of volume flow rates at multiple inlets and outlets. The RBCs are modelled as Lagrangian membranes using a finite element method (FEM). The fluid structure interaction (FSI) between the flow and the RBC membranes is realised using the immersed-boundary method (IBM) [9], which tackles the velocity interpolation and force spreading. The algorithm integrating the LBM, FEM and IBM [10] is implemented in the open-source blood flow simulation software *HemeLB* (`https://github.com/hemelb-codes/hemelb`) [11] for parallel computing.

## S1.1 Material model of RBC membrane

Each RBC is modelled as a closed membrane consisting of $N_f$ triangular facets and present a discocyte shape at rest [3]. The mesh resolution of the membrane (namely $N_f$) matches the lattice size $\Delta x$ of the flow domain for numerical stability and accuracy (see [12] for a detailed numerical analysis). The RBC membrane is hyperelastic, isotropic and homogeneous. Its mechanical properties are controlled by several moduli ($\kappa_s$, $\kappa_b$, $\kappa_\alpha$, $\kappa_A$, $\kappa_V$) governing energy contributions from strain, bending, area and volume of the membrane (see Table S2). Enclosed by the RBC membrane is the cytosol treated as a Newtonian fluid of plasma viscosity. The viscosity of the RBC membrane itself is not considered in the present material model.

The morphological deformation of an RBC in small vessels or channels are known to be dominated by the strain modulus $\kappa_s$ and the bending modulus $\kappa_b$, both of which have been extensively measured for healthy human RBCs using diverse experimental techniques. The commonly accepted values from different experiments are $\kappa_s = 5.5 \pm 3.3\,\mu$N/m and $\kappa_b = 1.15 \pm 0.9 \times 10^{-19}$ Nm, respectively (see reviews [13] and [14]). However, because these measurements all rely on certain deformation protocols that do not necessarily reflect the complex microcirculatory conditions, the obtained values may not apply to RBCs travelling in capillary networks of the mouse retina. Indeed, we find that the $\kappa_s$ and $\kappa_b$ required to maintain the integrity of the RBC membrane in our cellular simulations

**Table S2. Key parameters of the RBC model.** The symbol "$\sim$" represents dimensionless simulation units. Please refer to [3] for full details of the RBC model.

| Parameter | Description | Value | Unit | Comment or reference |
|---|---|---|---|---|
| $r_{rbc}$ | RBC radius | 4 | $\mu$m | [13] |
| $A_{rbc}$ | RBC surface | 140 | $\mu$m$^2$ | [13] |
| $V_{rbc}$ | RBC volume | 100 | $\mu$m$^3$ | [13] |
| $\eta_{plasma}$ | plasma viscosity | 1 | mPa s | modelled as liquid water |
| $\eta_{cytosol}$ | artificial cytosol viscosity | 1 | mPa s | assuming $\eta_{cytosol} = \eta_{plasma}$ |
| $\Gamma_{nominal}$ | Föppl-von Kármán number | 400 | – | $\Gamma_{nominal} = \frac{\kappa_s r_{rbc}^2}{\kappa_b}$ |
| $N_f$ | number of facets | 1280 | – | $N_f = 20(\frac{r_{rbc}}{\Delta x})^2$ |
| $\kappa_s$ | strain modulus | 50 | $\mu$N/m | resisting in-plane shearing |
| $\kappa_b$ | bending modulus | $2\times10^{-18}$ | Nm | resisting off-plane bending |
| $\tilde{\kappa}_\alpha$ | dilation modulus | 0.5 | – | conserving local area |
| $\tilde{\kappa}_A$ | surface modulus | 1 | – | conserving RBC surface |
| $\tilde{\kappa}_V$ | volume modulus | 1 | – | conserving RBC volume |

are roughly one order larger in magnitude than the reported values (see the simulation values in Table S2). This substantial increase in required $\kappa_s$ and $\kappa_b$ for reasonable RBC morphology may also arise from the intrinsic difference in the haemodynamic environment (*e.g.* magnitude ranges of the shear rate and wall shear stress) of the microcirculation system between mice and humans.

## S1.2 Boundary conditions for RBC simulation in ROIs

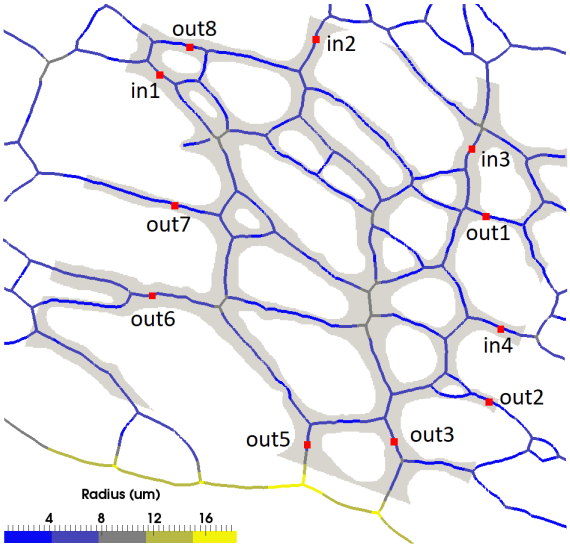


**Fig. S2. Boundary conditions for RBC simulation in ROI-1**. The imposed inflow/outflow and pressure conditions are specified according to the whole-plexus simulation based on generalised non-Newtonian blood rheology (Fig. S1c).

**Table S3. Boundary conditions for RBC simulations in designated subsets of the retinal network, namely ROI-1, ROI-2, ROI-3 and ROI-4 as illustrated in Fig. 1a.** $\hat{u}$ represents the centreline velocity at the selected cross-section (circular) of a given vessel that serves as the inlet/outlet of the ROI and $p$ is a reference pressure. $\hat{u}$ is set as positive for inlets and negative for outlets.

| ROI | Inlet/Outlet | Boundary type | Value | Unit | $D_{vessel}$ ($\mu$m) |
|---|---|---|---|---|---|
| 1 | $\hat{u}_{in1}$ | velocity | 0.500 | mm/s | 10.3 |
| | $\hat{u}_{in2}$ | velocity | 7.109 | mm/s | 9.2 |
| | $\hat{u}_{in3}$ | velocity | 5.511 | mm/s | 10.6 |
| | $\hat{u}_{in4}$ | velocity | 6.371 | mm/s | 7.2 |
| | $\hat{u}_{out1}$ | velocity | -0.0486 | mm/s | 3.7 |
| | $\hat{u}_{out2}$ | velocity | -0.376 | mm/s | 7.2 |
| | $\hat{u}_{out3}$ | velocity | -10.739 | mm/s | 5.9 |
| | $\hat{u}_{out4}$ | velocity | -2.356 | mm/s | 9.7 |
| | $\hat{u}_{out5}$ | velocity | -0.709 | mm/s | 13.5 |
| | $\hat{u}_{out6}$ | velocity | -0.446 | mm/s | 11.2 |
| | $p_{out7}$ | pressure | 0 | mmHg | 7.2 |
| 2 | $\hat{u}_{in1}$ | velocity | 11.710 | mm/s | 8.0 |
| | $\hat{u}_{in2}$ | velocity | 3.756 | mm/s | 15.7 |
| | $\hat{u}_{out1}$ | velocity | -0.774 | mm/s | 5.4 |
| | $\hat{u}_{out2}$ | velocity | -6.164 | mm/s | 10.6 |
| | $\hat{u}_{out3}$ | velocity | -5.209 | mm/s | 7.1 |
| | $\hat{u}_{out4}$ | velocity | -4.829 | mm/s | 10.4 |
| | $p_{out5}$ | pressure | 0 | mmHg | 14.5 |
| 3 | $\hat{u}_{in1}$ | velocity | 1.171 | mm/s | 7.1 |
| | $\hat{u}_{in2}$ | velocity | 10.277 | mm/s | 13.5 |
| | $\hat{u}_{in3}$ | velocity | 0.049 | mm/s | 6.9 |
| | $\hat{u}_{in4}$ | velocity | 0.002 | mm/s | 2.4 |
| | $\hat{u}_{out1}$ | velocity | -14.913 | mm/s | 8.8 |
| | $\hat{u}_{out2}$ | velocity | -30.298 | mm/s | 4.7 |
| | $p_{out3}$ | pressure | 0 | mmHg | 2.2 |
| 4 | $\hat{u}_{in1}$ | velocity | 4.222 | mm/s | 19.0 |
| | $\hat{u}_{in2}$ | velocity | 1.201 | mm/s | 5.5 |
| | $\hat{u}_{in3}$ | velocity | 6.367 | mm/s | 7.8 |
| | $\hat{u}_{out1}$ | velocity | -11.658 | mm/s | 10.3 |
| | $\hat{u}_{out2}$ | velocity | -7.182 | mm/s | 8.6 |
| | $\hat{u}_{out3}$ | velocity | -0.514 | mm/s | 7.3 |
| | $\hat{u}_{out4}$ | velocity | -0.113 | mm/s | 6.8 |
| | $p_{out5}$ | pressure | 0 | mmHg | 8.9 |

## S1.3 Benchmark simulations of RBC dynamics

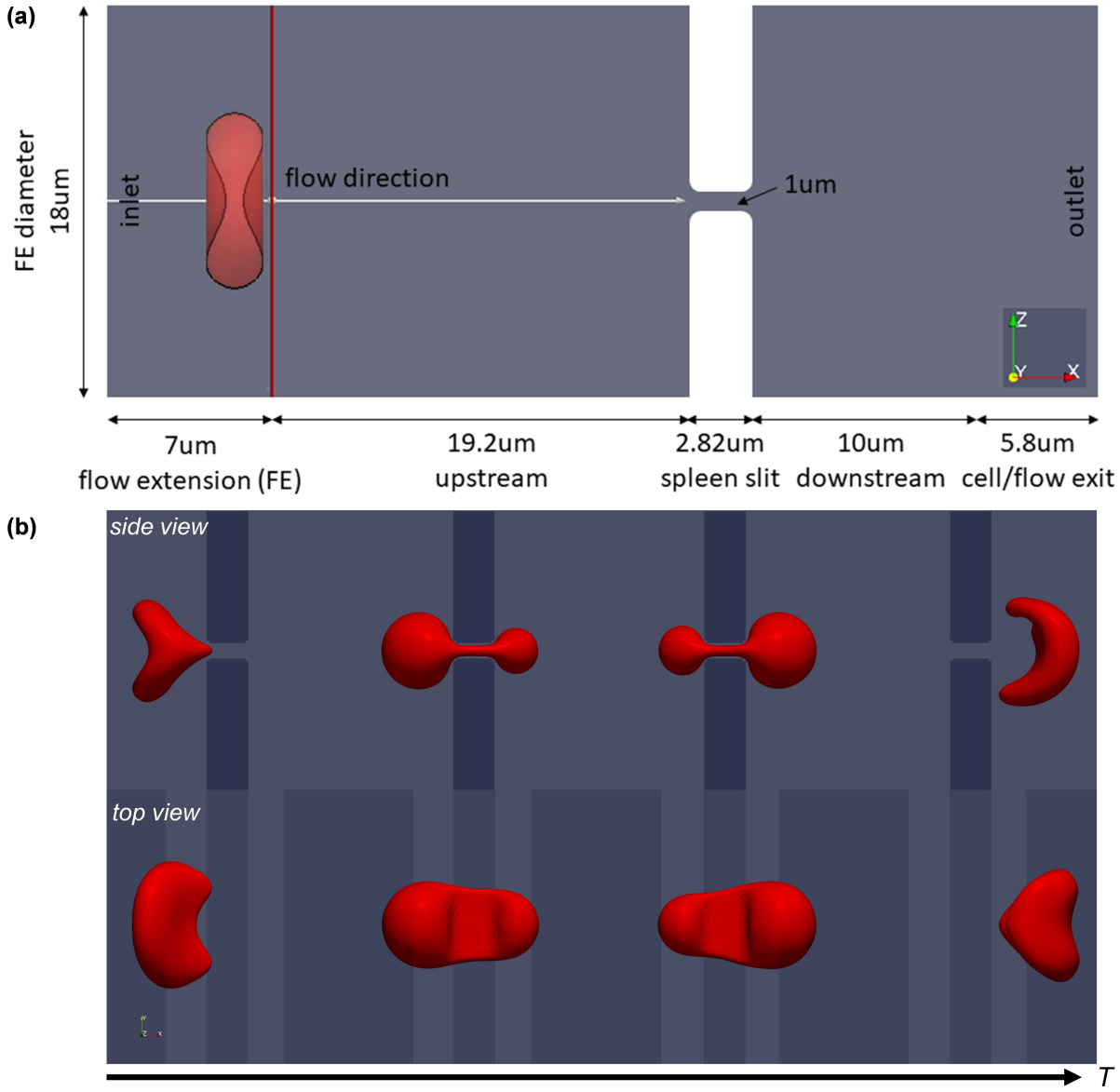


**Fig. S3. Benchmark test of a single RBC squeezing through a narrow slit.** (a) Model configuration. (b) Time-sequence of the RBC. From left to right: $t_1 = 80ms$, $t_2 = 87ms$, $t_3 = 100ms$, $t_4 = 111ms$.

Given that the RBCs (subject to the material model of the cell membrane) can be more demanding to resolve than the plasma flow in narrow vessels of the retinal network, we performed two benchmark tests to ensure that a resolution of $\Delta x = 0.5\,\mu$m (which was adopted for the whole-plexus simulation) is also suitable for the cellular simulation in ROI subsets. Because the smallest capillaries we encounter in the extracted ROIs are in the range of 2–3 $\mu m$, the choice of $\Delta x = 0.5\,\mu$m would lead to a minimum of 4–6$\Delta x$ across all vessel diameters. To test an extreme case for the RBC's deformation and motion, the first benchmark simulation considers a single RBC confronted by an exceedingly confined slit channel (by placing the cell up-front) of 1 $\mu m$ in depth, with only 6$\Delta x$ ($\Delta x = 0.17\,\mu$m

here) across the narrowest dimension (Fig. S3a). Smooth transit of the RBC is achieved under sufficiently large flow rates, where the cell can perform excessive deformation to squeeze into and then escape from the slit channel (Fig. S3b). More details about the model configuration and simulation results can be found in Sec. S1.3.

A second benchmark simulation is repeating the RBC simulation in ROI-4 (see Fig. 1a) under equivalent flow conditions after refining the voxel refined by two times, *i.e.* $\Delta x' = 0.25\,\mu$m. As dictated by the diffusive scaling for mitigating comprehensibility error in simulation, with the voxel size reduced by half, the new time step length also needs to be modified as one fourth of that of the original simulation (*i.e.* $\Delta t' = 1.04 \times 10^{-8}s$, $\Delta t = 4.17 \times 10^{-8}s$ for $\Delta x = 0.5\,\mu$m), meaning quadrupled simulation time (in time steps) for equivalent physical time (in seconds). The distribution of RBCs in the network is then compared with equivalent time steps of the original simulation with $\Delta x = 0.5\,\mu$m. Regardless of the random initialisation of cells for each simulation at the inlets, the time-sequence of RBC snapshots from the two simulation suggests that the case with coarser lattice resolution $\Delta x' = 0.5\,\mu$m satisfactory preserves the spatio-temporal RBC dynamics within the ROI network (*e.g.* their motion and distribution) as would be expected by that by $\Delta x = 0.25\,\mu$m (Fig. S4).

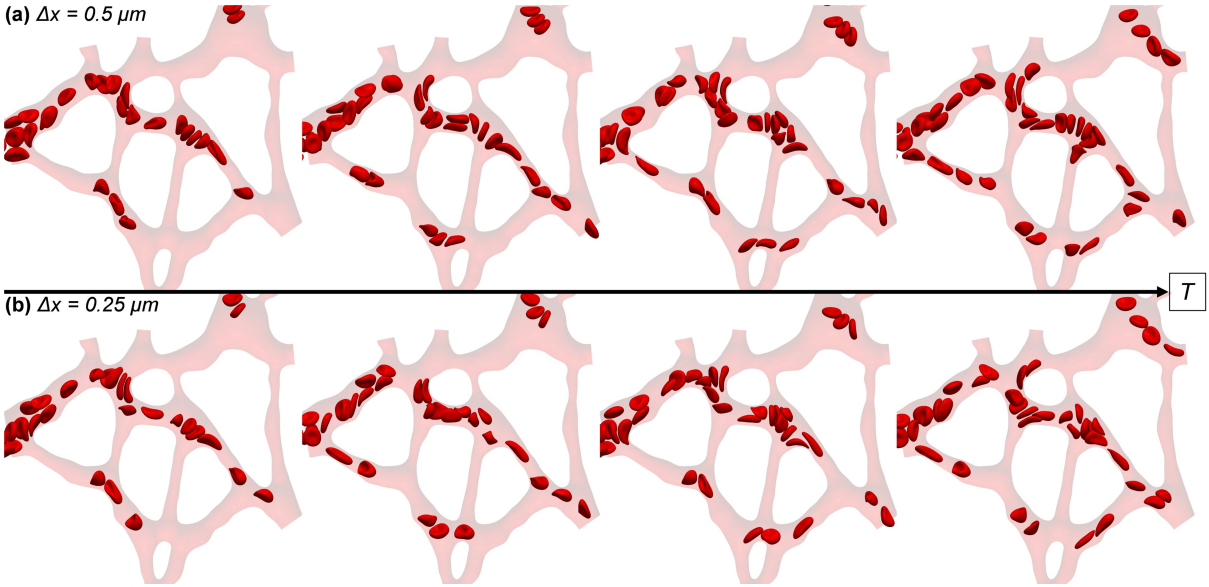


**Fig. S4. Comparison of simulated RBC dynamics in ROI-4 with (a) $\Delta x = 0.5\,\mu$m and (b) $\Delta x = 0.25\,\mu$m.** Time-sequence of the RBC motion (from left to right): $t_1 = 0.042s$, $t_2 = 0.046s$, $t_3 = 0.050s$, $t_4 = 0.054s$. Note that the initialisation of RBCs at the inlets are random (*i.e.* not identical for each simulation), causing a certain level of variation in cell number and morphology between simulations at equivalent time instants.

**Table S4. Errors of empirical prediction by the phase separation model [15] in comparison to our simulation data.** "ROI" represents region of interest; "BOI" represents bifurcation of interest; "CB" represents child branch. "L" and "S" refer to the relatively larger and smaller child branch within each bifurcation, respectively.

| ROI | CB | BOI-1 | BOI-2 | BOI-3 | BOI-4 | BOI-5 | BOI-6 | – | – |
|---|---|---|---|---|---|---|---|---|---|
| 2 | L | 0.44% | 0.22% | 2.38% | 0.0% | 0.0% | 1.12% | – | – |
| 2 | S | 2.26% | 3.47% | 0.0% | 2.89% | 1.7% | 0.0% | – | – |
| ROI | CB | BOI-15 | BOI-16 | BOI-17 | BOI-18 | BOI-19 | BOI-20 | BOI-21 | BOI-22 |
| 3 | L | 6.78% | 1.16% | 3.49% | 1.64% | 3.03% | 1.3% | 11.86% | 1.58% |
| 3 | S | 5.28% | 0.0% | 9.02% | 0.0% | 2.78% | 0.0% | 17.62% | 0.44% |
| ROI | CB | BOI-7 | BOI-8 | BOI-9 | BOI-10 | BOI-11 | BOI-12 | BOI-13 | BOI-14 |
| 4 | L | 2.32% | 1.35% | 4.74% | 0.28% | 0.0% | 2.5% | 1.21% | 0.72% |
| 4 | S | 2.68% | 0.0% | 9.19% | 1.08% | 0.0% | 1.97% | 4.29% | 0.0% |

# S2 Evaluation of simulation against empirical model

Several models have been established to describe the phenomenon of plasma skimming [16-19]. Among others, the most widely-applied one is probably the empirical phase-separation model (hereafter referred to as PSM) developed by Pries and co-workers based on *in vivo* experiments and theoretical modelling [15-16,20-22]. We follow the PSM formulation in [15,21]:

$$A = -13.29[(D_\alpha^2/D_\beta^2 - 1)/(D_\alpha^2/D_\beta^2 + 1)](1 - H_D)/D_F \tag{S1}$$

$$B = 1 + 6.98(1 - H_D)/D_F \tag{S2}$$

$$X_0 = 0.964(1 - H_D)/D_F \tag{S3}$$

wherein $D_\alpha$, $D_\beta$ and $D_F$ are diameters of the two child branches and the parent branch (evaluated in $\mu$m), respectively. $H_D$ is the discharge haematocrit of the parent branch.

With $D_\alpha$, $D_\beta$ and $D_F$ measured from the vascular geometry and $H_D$ obtained from the simulation (*via* an automated RBC-counting procedure), $A$, $B$, $X_0$ can be calculated individually for each bifurcation and the empirical curves are plotted as $FQ_E$ versus $FQ_B$. Equivalently, the simulation data are plotted in the form of $Q^*_{rbc}$ versus $Q^*_{blood}$ for comparison with the empirical predictions.

To evaluate the potential effect of cell volume difference as proposed in [23] between our RBC model (100 fl in volume) and realistic mouse RBCs (about 56.51 fl in volume), empirical predictions with rescaled fitting parameters $A'$, $B'$, $X_0{}'$ are also examined:

$$A' = -10.99[(D_\alpha^2/D_\beta^2 - 1)/(D_\alpha^2/D_\beta^2 + 1)](1 - H_D)/D_F \tag{S4}$$

$$B' = 1 + 5.77(1 - H_D)/D_F \tag{S5}$$

$$X_0{}' = 0.797(1 - H_D)/D_F \tag{S6}$$

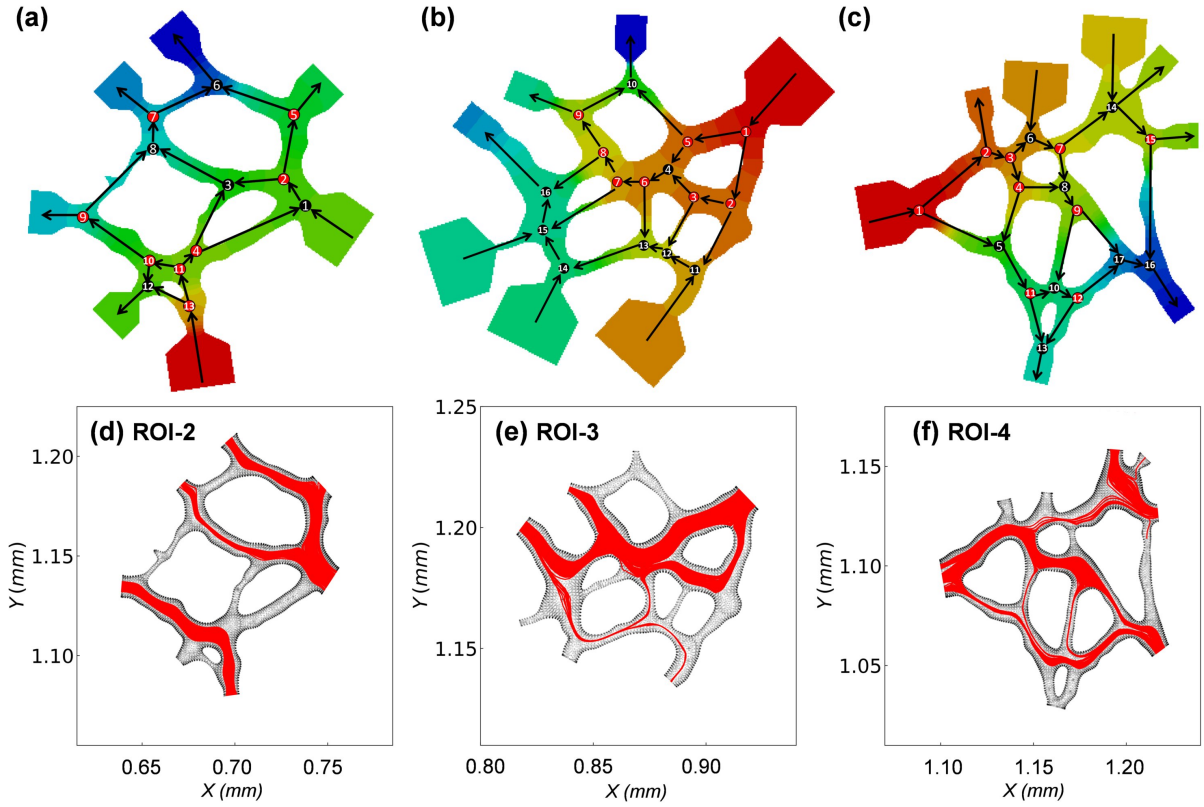


**Fig. S5. Quantification of RBC flow in selected regions of interest (ROIs).** (**a**–**c**) Flow patterns detected within ROI-2, ROI-3 and ROI-4, respectively. The arrows within the ROIs indicate the flow directions in individual vessel segments, and the background contour indicates the pressure field, with warmer colours (*e.g.* red) for higher pressures. The divergent bifurcations within each ROI are marked with red circles and the convergent confluences with black. (**d**–**f**) Combined cell trajectories in the ROIs throughout RBC simulations lasting for 0.33 s each.

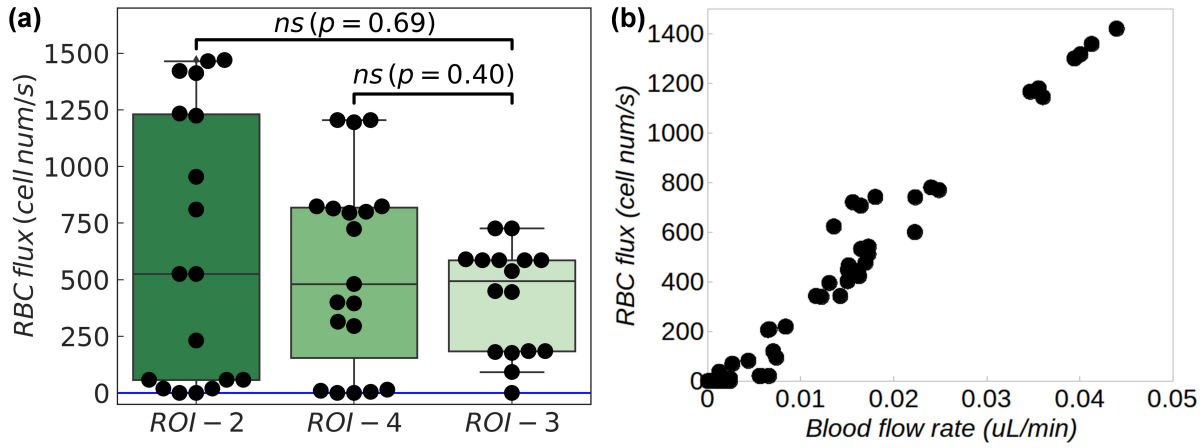


**Fig. S6. (a) Statistical test of time-average RBC flux for the lumenised vessels in ROI-2, ROI-4 and ROI-3. Two-sided Mann–Whitney U test is performed. The sample size is $n = 18, 19, 16$. (b) Relationship between RBC flux and blood flow rate for vessels extracted from bifurcations in ROI-2, ROI-3 and ROI-4 as in Fig. S5.**

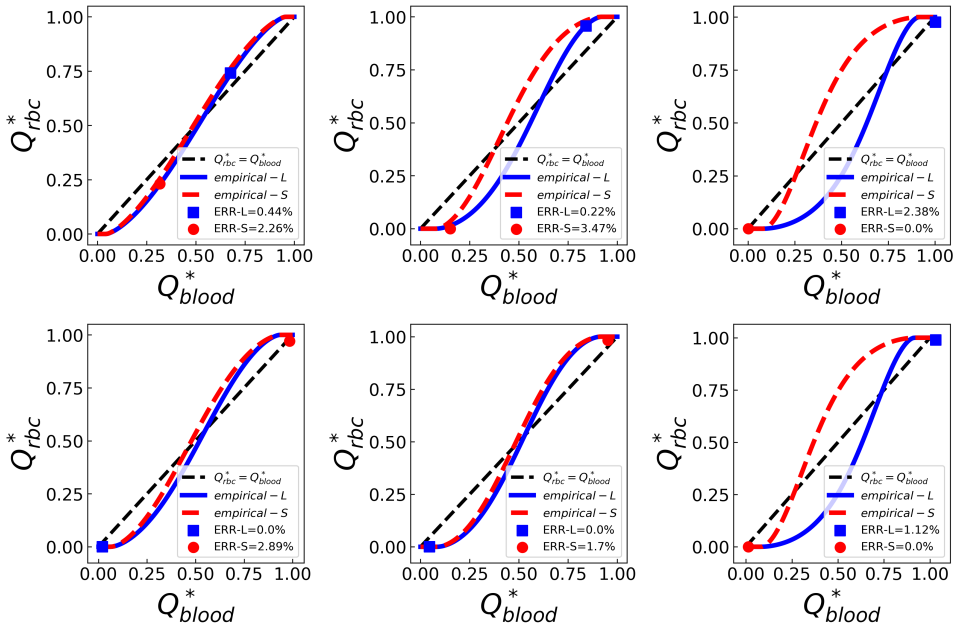


**Fig. S7. Evaluation of simulation data against empirical predictions by the phase separation model [15].** Simulation data extracted from divergent bifurcations in ROI-2 (see Fig. S5d) are plotted as fractional RBC flux $Q^*_{rbc}$ against fractional blood flow $Q^*_{blood}$. The simulation data are represented by squares/circles and the empirical predictions by solid lines. In each bifurcation, the relatively larger child branch is termed "L" and relatively smaller child branch termed "S". The black dashed line represent a linear hypothesis for $Q^*_{rbc}$ and $Q^*_{blood}$ in the absence of plasma skimming.

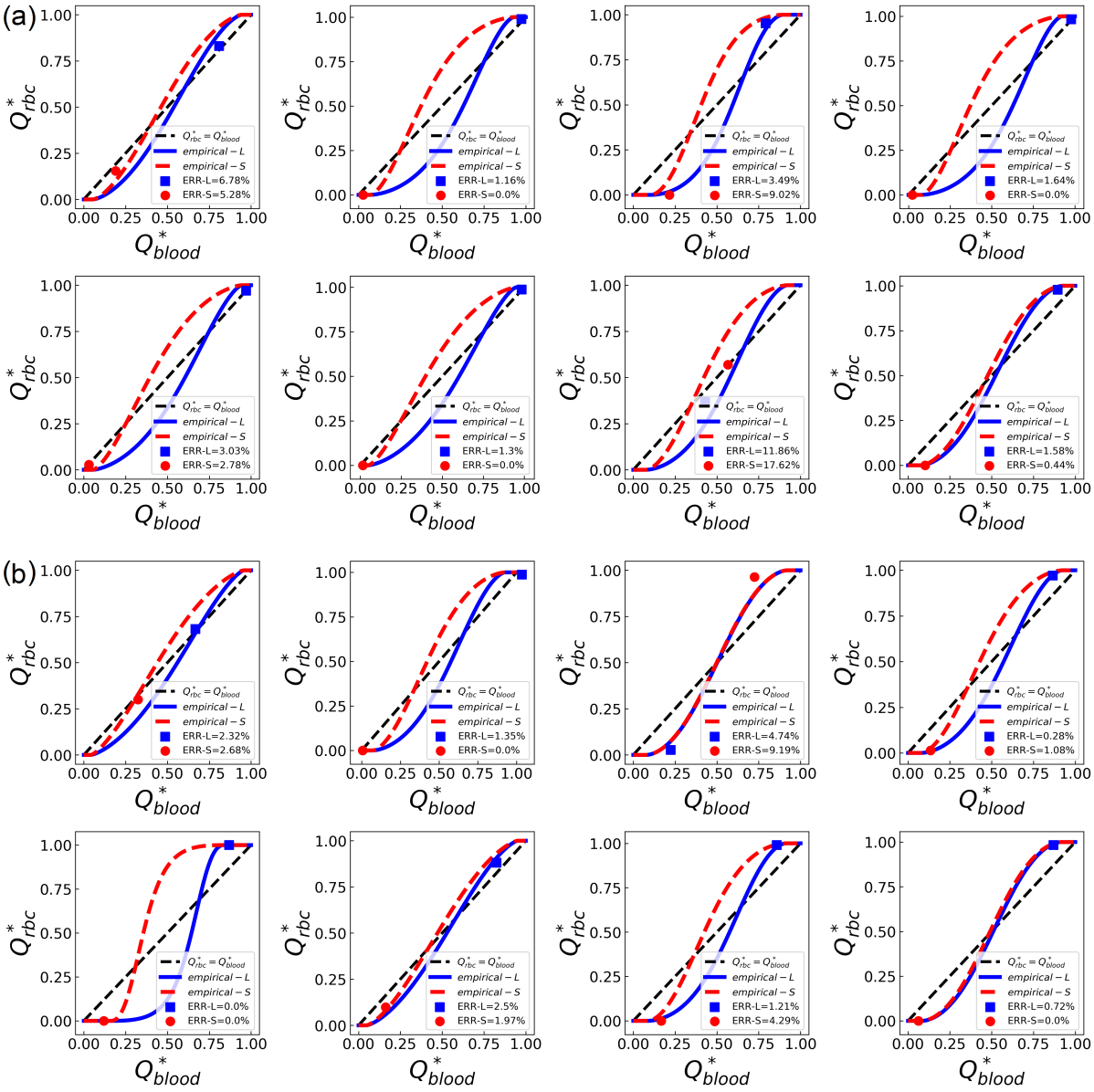


**Fig. S8. Evaluation of simulation data against empirical predictions.**. (a) Same conventions as Fig. S7, except for ROI-3 (see Fig. S5e).(b) Same conventions as Fig. S7, except for ROI-4 (see Fig. S5f).

**Table S5. Same conventions as Table S4, except that the phase separation model here adopts revised parameters $A'$, $B'$, ${X_0}'$ based on [15].** $A'$, $B'$, ${X_0}'$ account for the RBC volume difference (see Equations (S4)–(S6)).

| ROI | CB | BOI-1 | BOI-2 | BOI-3 | BOI-4 | BOI-5 | BOI-6 | – | – |
|---|---|---|---|---|---|---|---|---|---|
| 2 | L | 0.93% | 1.94% | 2.38% | 0.0% | 0.0% | 1.12% | – | – |
| 2 | S | 0.85% | 1.89% | 0.0% | 2.89% | 1.7% | 0.0% | – | – |
| ROI | CB | BOI-15 | BOI-16 | BOI-17 | BOI-18 | BOI-19 | BOI-20 | BOI-21 | BOI-22 |
| 3 | L | 8.54% | 1.16% | 0.49% | 1.64% | 3.03% | 1.3% | 15.15% | 2.07% |
| 3 | S | 7.04% | 0.0% | 5.94% | 0.0% | 2.78% | 0.0% | 20.9% | 0.04% |
| ROI | CB | BOI-7 | BOI-8 | BOI-9 | BOI-10 | BOI-11 | BOI-12 | BOI-13 | BOI-14 |
| 4 | L | 2.3% | 1.35% | 2.55% | 1.64% | 0.0% | 4.03% | 0.15% | 1.44% |
| 4 | S | 2.54% | 0.0% | 6.54% | 0.26% | 0.0% | 3.44% | 2.35% | 0.0% |

# S3 Asymmetry of velocity profile in RBC flow

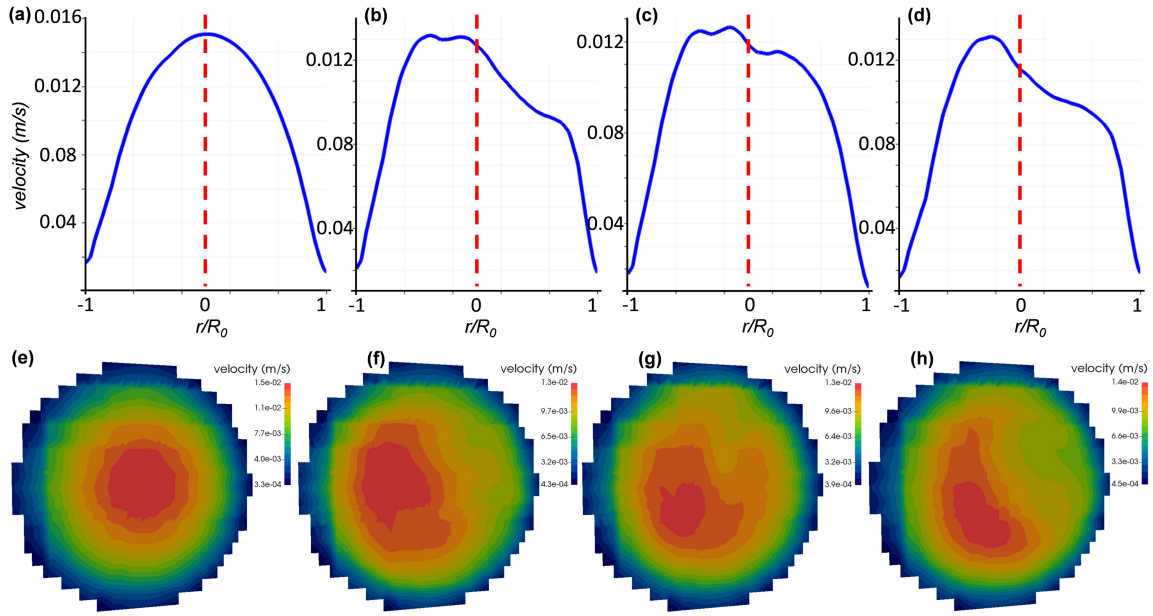


**Fig. S9. Temporal velocity profile and flow pattern in the RBC flow.** (**a-d**) Velocity profiles over time at the red solid line labelled in Fig. 6d. (**e-h**) Corresponding cross-sectional velocity contours at the same position. (a) and (e): $t_1 = 0.042$s. (b) and (f): $t_2 = 0.125$s. (c) and (g): $t_3 = 0.208$s. (d) and (h): $t_4 = 0.291$s.

# S4 Supplementary movies

**Movie S1.** Simulated RBC flow in region of interest ROI-1 of the retinal vasculature.
**Movie S2.** Simulated RBC flow in region of interest ROI-2 of the retinal vasculature.
**Movie S3.** Simulated RBC flow in region of interest ROI-3 of the retinal vasculature.
**Movie S4.** Simulated RBC flow in region of interest ROI-4 of the retinal vasculature.

# S5 Supplementary references


[1] Boyd J, Buick JM, Green S. 2007 Analysis of the Casson and Carreau-Yasuda Non-Newtonian Blood Models in Steady and Oscillatory Flows Using the Lattice Boltzmann Method. *Physics of Fluids* **19**(9), 093103.
[2] Bernabeu MO, Jones ML, Nielsen JH, Krüger T, Nash RW, Groen D, et al. 2014 Computer Simulations Reveal Complex Distribution of Haemodynamic Forces in a Mouse Retina Model of Angiogenesis. *Journal of The Royal Society Interface* **11**(99), 20140543.
[3] Krüger T. 2012 *Computer Simulation Study of Collective Phenomena in Dense Suspensions of Red Blood Cells under Shear.* Vieweg+Teubner Verlag, Wiesbaden.
[4] Qian YH, D'Humières D, Lallemand P. 1992 Lattice BGK Models for Navier-Stokes Equation. *EPL (Europhysics Letters)* **17**(6), 479.
[5] Bhatnagar PL, Gross EP, Krook M. 1954 A Model for Collision Processes in Gases.I. Small Amplitude Processes in Charged and Neutral One-Component Systems. *Physical Review* **94**(3), 511–525.
[6] Guo Z, Zheng C, Shi B. 2002 Discrete Lattice Effects on the Forcing Term in the Lattice Boltzmann Method. *Physical Review E* **65**(4), 046308.
[7] Bouzidi M, Firdaouss M, Lallemand P. 2001 Momentum Transfer of a Boltzmann-Lattice Fluid with Boundaries. *Physics of Fluids* **13**(11), 3452–3459.
[8] Ladd AJC. 1994 Numerical Simulations of Particulate Suspensions via a Discretized Boltzmann Equation. Part 1. Theoretical Foundation. *Journal of Fluid Mechanics* **271**, 285–309.
[9] Peskin CS. 2002 The Immersed Boundary Method. *Acta Numerica* **11**, 479–517.
[10] Zhou Q, Fidalgo J, Calvi L, Bernabeu MO, Hoskins PR, Oliveira MSN, et al. 2020 Spatiotemporal Dynamics of Dilute Red Blood Cell Suspensions in Low-Inertia Microchannel Flow. *Biophysical Journal* **118**(10), 2561–2573.
[11] Mazzeo MD, Coveney PV. 2008 HemeLB: A High Performance Parallel Lattice-Boltzmann Code for Large Scale Fluid Flow in Complex Geometries. *Computer Physics Communications* **178**(12), 894–914.
[12] Krüger T, Varnik F, Raabe D. 2011 Efficient and Accurate Simulations of Deformable Particles Immersed in a Fluid Using a Combined Immersed Boundary Lattice Boltzmann Finite Element Method. *Computers & Mathematics with Applications* **61**(12), 3485–3505.
[13] Lim GHW, Wortis M, Mukhopadhyay R. 2009 Red Blood Cell Shapes and Shape Transformations: Newtonian Mechanics of a Composite Membrane: Sections 2.1–2.4 In: *Soft Matter.* John Wiley & Sons, Ltd., pp. 83–139.
[14] Tomaiuolo G. 2014 Biomechanical Properties of Red Blood Cells in Health and Disease towards Microfluidics. *Biomicrofluidics* **8**(5), 051501.
[15] Pries AR, Reglin B, Secomb TW. 2003 Structural Response of Microcirculatory Networksto Changes in Demand: Information Transfer by Shear Stress. *American Journal of Physiology - Heart and Circulatory Physiology* **284**(6), H2204–H2212.
[16] Pries AR, Ley K, Claassen M, Gaehtgens P. 1989 Red Cell Distribution at Microvascular Bifurcations. *Microvascular Research* **38**(1), 81–101.

[17] Guibert R, Fonta C, Plouraboué F. 2010 A New Approach to Model Confined Suspensions Flows in Complex Networks: Application to Blood Flow. *Transport in Porous Media* **83**(1), 171–194.
[18] Gould IG, Linninger AA. 2015 Hematocrit Distribution and Tissue Oxygenation in Large Microcirculatory Networks. *Microcirculation* **22**(1), 1–18.
[19] Lee TR, Yoo SS, Yang J. 2017 Generalized Plasma Skimming Model for Cells and Drug Carriers in the Microvasculature. *Biomechanics and Modeling in Mechanobiology* **16**(2), 497–507.
[20] Pries AR, Secomb TW, Gaehtgens P, Gross JF. 1990 Blood Flow in Microvascular Networks. Experiments and Simulation. *Circulation Research* **67**(4), 826–834.
[21] Pries AR, Secomb TW. 2005 Microvascular Blood Viscosity in Vivo and the Endothelial Surface Layer. *American Journal of Physiology - Heart and Circulatory Physiology* **289**(6), H2657–H2664.
[22] Rasmussen PM, Secomb TW, Pries AR. 2018 Modeling the Hematocrit Distribution in Microcirculatory Networks: A Quantitative Evaluation of a Phase Separation Model. *Microcirculation* **25**(3), e12445.
[23] Lorthois S, Cassot F, Lauwers F. 2011 Simulation Study of Brain Blood Flow Regulation by Intra-Cortical Arterioles in an Anatomically Accurate Large Human Vascular Network: Part I: Methodology and Baseline Flow. *NeuroImage* **54**(2), 1031–1042.